Indian Journal of Pure & Applied Physics
Vol. 64, November 2026, pp. 1181-1191
DOI: 10.56042/ijpap.v64i11.31219

Structure–Property Correlation in $Co_xFe_{(3-x)}O_4$ Spinel Nano-Ferrites: Influence of Lattice Contraction on Elastic and Magnetic Properties

Mohd Bilal Siddiqui* & Ashok Kumar Dimri

Department of Physics, Maharaj Singh College, Saharanpur 247 001, India

(Affiliated to Chaudhary Charan Singh University, Meerut, India)

Received: 6th May 2026; accepted: 12th October 2026

The sol–gel auto-combustion method is used to synthesize $Co_xFe_{(3-x)}O_4$ (x = 0.50, 0.55, 0.60) nanoparticles and calcined at 600 °C. Using X-ray diffraction (XRD) analysis, the formation of a single-phase cubic spinel structure is confirmed. Increasing cobalt concentration (x = 0.50 to 0.60) resulted in a reduction of the lattice parameter from 8.383 Å to 8.313 Å, accompanied by a decrease in average crystallite size from 46.2 nm to 27.7 nm and an increase in microstrain from 0.25×10^{-3} to 0.52×10^{-3}. This unit cell contraction directly influenced the elastic properties, with calculated Young's modulus increasing from 122.03 GPa to 123.03 GPa and estimated bulk modulus from 84.5 GPa to 85.2 GPa. Based on Néel's two-sublattice model, theoretically estimated net magnetic moment showed a slight reduction (4.0 μB to 3.8 μB) along with estimated saturation magnetization (95.84 emu/g to 90.93 emu/g), whereas the estimated Curie temperature increased from 745.34 K to 772.18 K due to stronger A–O–B super-exchange interactions. Morphological study via FE-SEM showed agglomerated grains (400–800 nm) indicating the formation of secondary particle clusters and EDX confirmed the expected elemental stoichiometry.

Keywords: Sol-gel auto-combustion, Cobalt ferrites, Lattice contraction, Micro-strain

1 Introduction

Spinel ferrites have attracted considerable attention due to their tunable electromagnetic properties, making them suitable for applications in microwave and magnetic devices[1]. Among them, cobalt-substituted ferrites ($Co_xFe_{(3-x)}O_4$) are of particular interest owing to their high magneto crystalline anisotropy, thermal stability, and chemical robustness. Cobalt (Co^{2+}) was selected as the substituting cation due to its ionic radius (0.745 Å for octahedral coordination) compared to iron ions (Fe^{3+}, 0.645 Å). This ionic size difference allows for systematic variation in lattice strain and inter-atomic bond lengths, providing a suitable matrix to investigate the effect of lattice contraction on structural and estimated physical properties while preserving the baseline cubic spinel phase. These properties are strongly influenced by the distribution of cations between tetrahedral (A) and octahedral (B) sites in the spinel structure[2,3]. Various synthesis routes have been employed for the preparation of spinel ferrites; however, the sol–gel auto-combustion method is widely preferred due to its ability to provide better compositional homogeneity, phase purity, and control over particle size at relatively lower processing temperatures[4,5]. While the structural and magnetic properties of cobalt ferrites have been widely reported, there is a significant gap in understanding the mechanical and elastic evolution of these materials under substitution-induced strain. Most studies focus purely on experimental magnetic measurements, often overlooking the underlying elastic constants that govern the structural stability of the spinel lattice. As cobalt ions are incorporated into the lattice, the unit cell undergoes contraction, which directly influences the inter-ionic distances and, consequently, the elastic moduli. Understanding this correlation is crucial, as the mechanical robustness of a ferrite determines its performance and durability in practical device applications. In particular, small variations in cobalt concentration (x = 0.50 to 0.60) can significantly influence lattice parameters, inter-ionic distances, and bond lengths, which in turn affect the mechanical stability and predicted magnetic behavior of the material. The concentration ranges of x = 0.50 to 0.60 was selected to examine this intermediate substitution regime, where systematic lattice contraction and microstrain can be evaluated without significant phase instability. The composition x = 0.50 serves as the starting baseline for this series.

*Corresponding author: E-mail: bilalsiddiqui09@gmail.com

In the present work, $Co_xFe_{(3-x)}O_4$ (x = 0.50, 0.55, 0.60) nano-ferrites were synthesized via the sol–gel auto-combustion method and calcined at 600 °C following reported thermal processing parameters[6]. A key highlight of this work is the mathematical correlation between lattice contraction and mechanical stiffness[7,8]. The elastic moduli (Young's modulus, Bulk modulus, etc.) were evaluated using experimental lattice parameters and further estimated the magnetic moments using Néel's two-sublattice model. By linking structural distortion with physical properties, this study provides a clear scientific justification for the observed trends, validated through comparison with established literature.

2 Experimental Details

2.1 Materials

For the synthesis of $Co_xFe_{(3-x)}O_4$(x = 0.50, 0.55, 0.60) nanoparticles, high-purity analytical grade (AR) chemicals were used without extra purification. Cobalt nitrate hexahydrate [$Co(NO_3)_2.6H_2O \geq 99$ % purity, Sigma-Aldrich] and ferric nitrate nonahydrate [$Fe(NO_3)_3.9H_2O \geq 99$ % purity, Sigma-Aldrich] served as the primary metal salt precursors, while citric acid [$C_6H_8O_7 \geq 99$ % purity, Sigma-Aldrich] was employed as the chelating agent. Double-distilled water was used as the solvent throughout the synthesis process.

2.2 Synthesis

Cobalt ferrite nanoparticles $Co_xFe_{(3-x)}O_4$ (x = 0.50, 0.55, 0.60) were synthesized using the sol–gel auto-combustion method[9,10]. Stoichiometric amounts of cobalt nitrate [$Co(NO_3)_2{\cdot}6H_2O$] and ferric nitrate [$Fe(NO_3)_3{\cdot}9H_2O$] were completely dissolved in high-purity double-distilled water under continuous magnetic stirring. Citric acid ($C_6H_8O_7$) was added in a 1:1 molar ratio relative to the total metal nitrate cations to serve as both a chelating agent and organic fuel. The pH of the precursor solution was adjusted to ~7.0 by the dropwise addition of an aqueous ammonia solution under constant stirring to promote metal-citrate complexation. The solution was continuously heated at 80 °C on a hot plate under continuous stirring until a dark, viscous gel was formed. Upon further heating at ~200 °C, a self-propagating auto-combustion reaction was initiated, producing a loose, fluffy ash precursor powder. Finally, the resulting powder was thoroughly ground using an agate mortar and calcined at 600 °C for 4 hours in a muffle furnace to obtain the desired single-phase crystalline spinel nano-ferrites. Structural, morphological, and elemental characterizations of the calcined samples were carried out using X-ray diffraction (XRD), field emission scanning electron microscopy (FE-SEM), and energy-dispersive X-ray spectroscopy (EDX), respectively. Furthermore, the obtained experimental data were utilized for the theoretical estimation of various mechanical and magnetic parameters. The overall sequence of the sol-gel auto combustion synthesis is illustrated schematically in Fig. 1.

2.3 Characterization Techniques

Using XRD the phase identification and structural parameters were analyzed (Rigaku, Japan) and using Field Emission Scanning Electron Microscopy

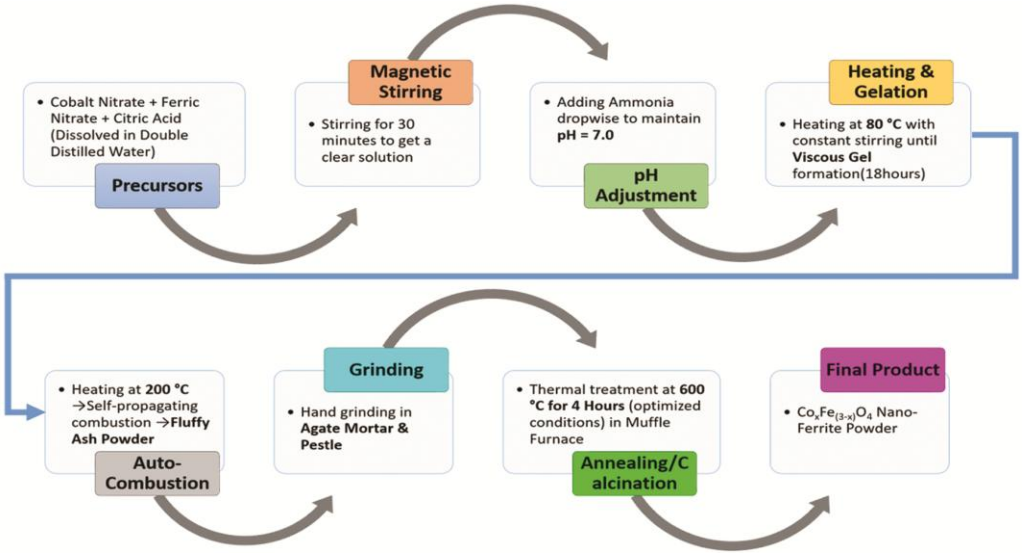

Fig. 1 — Process of Sol-Gel Auto-Combustion synthesis of $Co_xFe_{(3-x)}O_4$ nanoparticles

(FE-SEM) and EDX (ZEISS Sigma, Germany) surface morphology and elemental composition were investigated. All these characterizations were carried out at the Sophisticated Instrument Centre (SIC), IIT Indore, India.

3 Results and Discussion

3.1 Structural Analysis (XRD)

3.1.1 Phase Identification

The XRD patterns confirm a single-phase cubic spinel structure for $Co_xFe_{(3-x)}O_4$ samples (S1, S2, and S3) presented in Fig. 2. The diffraction peaks are indexed to the (220), (311), (400), (422), (511), and (440) planes, the results verify that high crystallinity without any impurity phases is achieved at 600 °C annealing temperature[11-13].

3.1.2 Structural Parameters Analysis

The diffraction-peak positions, full widths at half maximum, interplanar spacings, and corresponding calculated lattice parameters are summarized in Table 1.

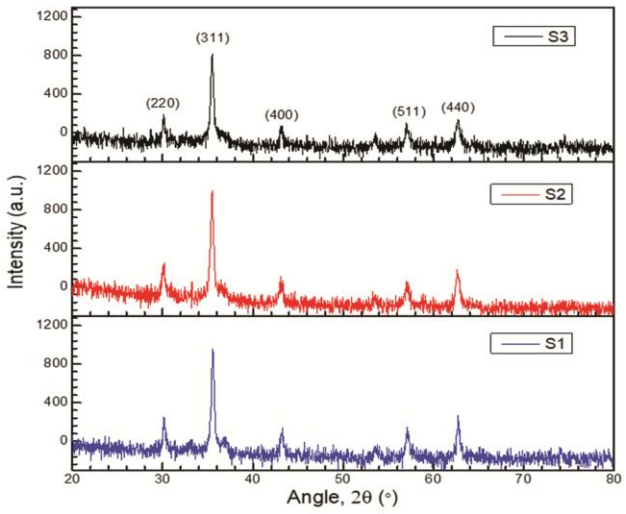

Fig. 2 — XRD patterns of the synthesized nano-ferrites calcined at 600 °C (optimized conditions)

3.1.3 Structural and Micro Structural Refinement

The structural properties of the synthesized ferrite nanoparticles were systematically investigated using Nelson-Riley (NR) refinement and Williamson-Hall (W-H) plots. Figure 3 (a) Nelson–Riley plot: F(θ) (x axis) versus $a_{(\theta)}$ (Å) (y axis) and Fig. 3 (b) Williamson–Hall plot: 4 sinθ (x axis) versus β cosθ (rad) (y axis).

Using Nelson-Riley and Williamson-Hall analysis, refined structural parameters were determined for $Co_xFe_{(3-x)}O_4$ (x = 0.50, 0.55, 0.60) nanoparticles.

To find refined lattice constant a plot is generated between Nelson Riley function F(θ) (X axis) and calculated lattice constant $a_{(\theta)}$ (Y axis) from XRD using relation;

$$a_{(\theta)} = m\,F(\theta) + a_0 \quad \text{... (1)}$$

where F(θ) *is* Nelson Riley function, $a_{(\theta)}$ *is* calculated lattice constant *and* a_0 *is* true value of lattice parameter.

Nelson Riley function *F(θ)* is defined as;

$$F(\theta) = \tfrac{1}{2}\left[\left(\cos^2\theta / \sin\theta\right) + \left(\cos^2\theta / \theta\right)\right] \quad \text{... (2)}$$

[14]

By extrapolating the linear fit to F(θ) = 0 (Fig. 3a), the refined lattice parameters were obtained. The results Table 2 show a gradual decrease in the lattice parameter from 8.383 Å to 8.313 Å with increasing cobalt concentration. This reduction is accompanied by a corresponding decrease in unit cell volume from 589.10 Å³ to 574.48 Å³, indicating compositional influence on the lattice structure.

Similarly, to find crystal size and microstain, Williamson-Hall curve is plotted between 4 sinθ (x axis) and β cosθ (y axis) (Fig. 3 (b)). Williamson–Hall (W–H) relation is;

$$\beta\cos\theta = (K\lambda / D) + 4\varepsilon\sin\theta, \quad \text{... (3)}$$

where β is full width at half maximum (FWHM), θ is the Bragg angle, K is the shape factor (0.9), and λ is the X-ray wavelength (1.5406 Å) given with XRD data[15].

Table 1 — Structural and lattice parameters of $Co_xFe_{(3-x)}O_4$ (x = 0.50, 0.55, 0.60) nanoparticles calcined at 600 °C (optimized conditions)

Samples x	2θº	Plane	FWHM(β) radians	4 sin θ	β cos θ	F(θ)	d(Å)	$a_{(\theta)}$ (Å)	D_{sch} (nm)
S_1	35.6	(311)	0.00488	1.2227	0.00465	5.084	2.519	8.3568	
x = 0.50	43.2	(400)	0.00558	1.4727	0.00519	3.261	2.092	8.3708	31.3
	62.7	(440)	0.00663	2.0811	0.00565	1.342	1.480	8.3749	
S_2	35.8	(311)	0.00558	1.2294	0.00531	5.029	2.506	8.3121	
x = 0.55	43.4	(400)	0.00628	1.4792	0.00584	3.226	2.083	8.3344	27.4
	63.0	(440)	0.00733	2.0899	0.00624	1.326	1.474	8.3394	
S_3	36.1	(311)	0.00628	1.2393	0.00597	4.947	2.486	8.2452	
x = 0.60	43.7	(400)	0.00698	1.4889	0.00649	3.175	2.070	8.2800	24.5
	63.4	(440)	0.00803	2.1017	0.00683	1.305	1.465	8.2923	

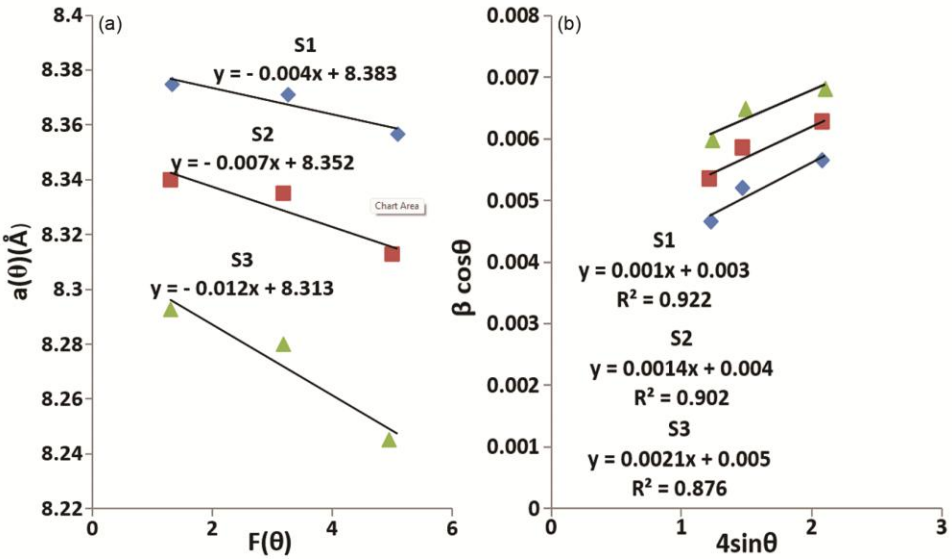

Fig. 3 — Structural refinement analysis of $Co_xFe_{(3-x)}O_4$ (x = 0.50, 0.55, 0.60) nano-ferrites calcined at 600 °C: (a) Nelson–Riley refinement plots for the determination of lattice parameters; and (b) Williamson–Hall plots for the estimation of crystallite size and microstrain

Table 2 — Refined structural parameters calcined at 600 °C (optimized conditions)

Samples x	Lattice Parameter a (Å)[NR Plot]	Crystallite Size D(nm) [WH plot]	Microstrain ε ×(10^{-3}) [WH plot]	Unit Cell VolumeV (Å^3)	Dislocation density (δ) ×(10^{15}) line/ m^2
0.50(S_1)	8.383	46.2	0.25	589.10	0.468
0.55(S_2)	8.352	34.7	0.35	582.60	0.831
0.60(S_3)	8.313	27.7	0.52	574.48	1.300

The W–H plots exhibit linear behavior (Y = mx + C), where the intercept provides the crystallite size and the slope yields the lattice strain. So;

$$D = 0.9\,\lambda / C \text{ and } m = \varepsilon \quad \ldots (4)$$

As summarized in Table 2, the crystallite size decreases from 46.2 nm to 27.7 nm with increasing cobalt substitution, indicating suppression of crystallite growth. In contrast, the microstrain (ε) increases from 0.25 × 10^{-3} to 0.52 × 10^{-3}, suggesting the development of lattice distortion and internal stress within the structure.

Furthermore, the dislocation density [$\delta = \frac{1}{D^2}$] increases from 0.468 × 10^{15} to 1.300 × 10^{15} lines/m², which is consistent with the reduction in crystallite size and increase in lattice strain[16-18]. These variations in structural parameters indicate that cobalt substitution influences the internal lattice environment and defect structure of the material.

3.2 Phenomenological Insights and Structure–Property Correlations

The compositional variation in $Co_xFe_{(3-x)}O_4$ (x = 0.50, 0.55, 0.60) leads to systematic changes in the lattice structure, which may influence the physical properties of the material. The observed unit cell contraction and variation in structural parameters provide useful insight into the relationship between composition and the internal lattice environment.

The surface-to-volume ratio (S/V) is an important parameter for nanomaterials, as it determines the fraction of atoms present at the surface, thereby influencing their physical properties[19]. For the synthesized $Co_xFe_{(3-x)}O_4$ nano-ferrites, the S/V ratio was calculated using the relation S/V = 6/D, where D represents the average crystallite size obtained from XRD analysis. With increasing cobalt substitution (x = 0.50 to 0.60), a systematic reduction in crystallite size from 46.2 nm to 27.7 nm is observed, resulting in an increase in the S/V ratio from 0.129 nm^{-1} to 0.216 nm^{-1}. This increase indicates a higher proportion of surface atoms at elevated substitution levels. The enhancement in surface-to-volume ratio reflects the structural refinement of the material and may influence surface-related properties, suggesting potential relevance for applications involving surface interactions.

3.2.1 Texture Coefficient and Structural Orientation

The crystalline orientation and the quality of the synthesized nano-ferrites were further investigated by calculating the texture coefficient (TC)[20]. The TC(hkl) for the most prominent (311) peak was determined to understand the growth preference of the grains. The calculation was performed using the following relation;

$$TC(kl) = \frac{I(hkl)/I_0(hkl)}{\frac{1}{N}\Sigma I(hkl)/I_0(hkl)} \quad \ldots (5)$$

I(hkl) and I_0(hkl) are observed and standard (JCPDS) intensities, respectively. The results are summarized in Table 3. Peak intensities were extracted using standard peak fitting methods.

The T_C(hkl) values for all three compositions (x = 0.50, 0.55, 0.60) were found to be near 1.0. This indicates that the grains are randomly oriented throughout the samples, confirming the isotropic nature of the polycrystalline spinel structure.

3.2.2 Structural Stability and Tolerance Factor Analysis

The structural stability and the degree of distortion in the cubic spinel lattice of $Co_xFe_{(3-x)}O_4$nanoparticles were evaluated using Goldschmidt's Tolerance Factor (t)[21]. This dimensionless parameter is a critical indicator of the geometrical stability of the crystal structure and is defined by the following relation;

$$t = \frac{r_0 + r_A}{\sqrt{2}(r_0 + r_B)} \quad \ldots (6)$$

For composition $Co_xFe_{(3-x)}O_4$ cation distribution is represented as $(Fe^{3+})_A$ $[Co^{2+}{}_x$ $Fe^{3+}{}_{2-x}]_B$ $O^{2-}{}_4$. To determine the structural parameters of the synthesized $Co_xFe_{(3-x)}O_4$ system, the effective ionic radii of the tetrahedral (r_A) and octahedral (r_B) sites were calculated. The calculations were based on the standard ionic radii values reported[22] where $r_{Fe}3+$ (Tetrahedral): 0.49 Å, $r_{Fe}{}^{3+}$ (Octahedral): 0.645 Å, $r_{Co}{}^{2+}$ (Octahedral): 0.745 Å, $r_o{}^{2-}$ (Oxygen ion): 1.32 Å. The calculated effective ionic radii and the corresponding Goldschmidt tolerance factors for all compositions are presented in Table 4.

Effective Radii Calculation

r_A=0.49 Å, r_0= 1.32 Å

$r_B = [x \times rCo^{2+} + (2\text{-}x) \times rFe^{3+}] / 2$

The calculated values of Goldschmidt's tolerance factor (t) for all the samples were found in the range of 0.643 to 0.639. Although these values deviate from the ideal unity (t=1), they fall well within the stable range for cubic spinel structures. The slight decrease in 't' with increasing cobalt substitution is attributed to the larger ionic radius of Co^{2+} (0.745 Å) replacing Fe^{3+} (0.645 Å) at the octahedral sites, which induces a controlled lattice distortion while maintaining structural integrity.

3.2.3 Influence of Unit Cell Contraction on Inter-Ionic Distances and Bond Lengths

To further investigate the impact of Cobalt substitution on the local environment of the spinel lattice, the hopping distances (L_A, L_B) and bond lengths (d_A, d_B) were evaluated. The calculated tetrahedral and octahedral hopping distances, together with the corresponding bond lengths, are listed in Table 5.

The hopping distances for both tetrahedral (L_A) and octahedral (L_B) sites show a downward trend[23]. The decrease in L_B is particularly significant as it suggests that the distance between neighboring metal ions at the octahedral sites is reducing. This contraction facilitates easier electronic exchange (hopping) between the cations, which can enhance the electrical properties of the material[24]. The analysis of structural parameters reveals that as the Cobalt concentration increases, the lattice constant (a) decreases, leading to a contraction of the unit cell. Concurrently, the oxygen parameter (u) shows a progressive increase

Table 4 — Calculated effective ionic radii for tetrahedral (r_A) and octahedral (r_B) sites, along with Goldschmidt's tolerance factor (t) for $Co_xFe_{(3-x)}O_4$nano-ferrites

Sample (x)	r_A (Å)	r_B (Å)	Tolerance Factor (t)
0.50 (S1)	0.49	0.670	0.643
0.55 (S2)	0.49	0.672	0.641
0.60 (S3)	0.49	0.675	0.639

Table 3 — Texture Coefficient calcined at 600 °C (optimized conditions)

Samples (x)	(hkl)	I(observed)	I_0(Standard)	$R = \frac{I}{I_0}$	T_C(hkl)
0.50 (S_1)	(311)	1000	100	10.00	1.01
	(440)	390	40	9.75	0.99
0.55 (S_2)	(311)	990	100	9.90	1.00
	(440)	400	40	10.00	1.01
0.60 (S_3)	(311)	880	100	8.80	0.98
	(440)	360	40	9.00	1.02

Table 5 — Geometrical Analysis (Hopping distances & Bond lengths) calcined at 600 °C (optimized conditions)

Samples x	Lattice Parameter a (Å)	Oxygen Parameter u	Hopping Distance		Bond length	
			L_A (Å)	L_B (Å)	d_A(Å)	d_B (Å)
0.50(S_1)	8.383	0.3810	3.630	2.954	1.902	2.062
0.55(S_2)	8.352	0.3815	3.616	2.944	1.901	2.049
0.60(S_3)	8.313	0.3821	3.599	2.930	1.900	2.037

Table 6 — Estimated elastic moduli calcined at 600 °C (optimized conditions)

Samples x	a (Å)	C_{11}(GPa)	C_{12}(GPa)	G(GPa)	B(GPa)	E(GPa)	Poisson's Ratio σ
0.50(S_1)	8.383	149.1	52.2	48.45	84.5	122.03	0.26
0.55(S_2)	8.352	149.6	52.4	48.60	84.8	122.41	0.26
0.60(S_3)	8.313	150.3	52.6	48.85	85.2	123.03	0.26

from 0.3810 to 0.3821, indicating an enhanced anion displacement due to the substitution of Co^{2+}in the inverse spinel lattice. Despite the increase in u, the tetrahedral bond length (d_A) exhibits a slight decrease (1.902 Å to 1.900 Å), confirming that the overall lattice contraction is the dominant factor. This reduction in bond lengths (d_A, d_B) correlates with the increased stiffness and higher elastic moduli observed in the samples. This trend confirms that the substitution of Cobalt ions into the ferrite matrix leads to a more densely packed crystal structure. The overall decrease in L and d values is a direct consequence of the shrinkage in the unit cell volume, ensuring a consistent and stable structural evolution in the $Co_xFe_{(3-x)}O_4$ system.

3.2.4 Elastic Properties Analysis

To understand the mechanical strength and inter-atomic bonding of the$Co_xFe_{(3-x)}O_4$ system, the elastic constants (C_{11}, C_{12}) and mechanical moduli were evaluated. The results are presented in Table 6.

The variation of elastic stiffness constants (C_{11}, C_{12}) and all Modulus with Cobalt content is shown in Table 6[7,8, 25]. It is evident that all parameters exhibit a consistent upward trend. This increase is a direct consequence of the unit cell contraction. As the lattice parameter (a) decreases, the inter-atomic distances (d_A, d_B) shorten, leading to stronger inter-ionic interactions. Mathematically, the inverse relationship between the elastic constants and the lattice parameter ($C \propto 1/a$) confirms that the structural shrinkage directly enhances the mechanical rigidity of the spinel lattice. The rise in Bulk Modulus (B) further signifies that the $Co_xFe_{(3-x)}O_4$ system becomes more resistant to uniform compression, making it a more robust ceramic material at higher Cobalt concentrations. The structural refinement observed via XRD suggests a strong correlation with magnetic behavior of these nanoparticles, highlighting their potential for high-performance magnetic applications. The calculated values of Poisson's ratio (σ) were found to be approximately 0.26 for all compositions. This value lies well within the standard range for spinel ferrites (typically 0.25 to 0.32), confirming the mechanical stability and structural integrity of the cubic spinel lattice.

Table 7 (a) — The geometrical bond angles (θ_1 to θ_5)

Angle	Coordination	Physical Meaning
θ_1	A-O-B	Primary Magnetic Coupling
θ_2	B-O-B	Octahedral Symmetry
θ_3	B-O-B	Structural Stability
θ_4	B-O-B	Intersite Interaction
θ_5	A-O-A	Tetrahedral Geometry

Table 7 (b) — The geometrical bond angles (θ_1 to θ_5) calculated for the spinel lattice calcined at 600 °C (optimized conditions)

Samples x	a(Å)	U	θ^o_1	θ^o_2	θ^o_3	θ^o_4	θ^o_5
0.50(S_1)	8.383	0.3810	121.35	93.68	146.50	76.22	102.15
0.55(S_2)	8.352	0.3815	121.11	93.89	146.54	76.27	102.19
0.60(S_3)	8.313	0.3821	120.78	94.25	146.60	76.35	102.25

3.2.5 Bond Angle Analysis and Lattice Symmetry

The local coordination geometry was analyzed by calculating five distinct bond angles ($\theta_1$to θ_5) based on the oxygen parameter (u)[26]. The geometrical assignments of these angles are given in Table 7 (a), while their calculated values for the three compositions are presented in Table 7(b).

The bond angle θ_1 (A-O-B) is a key parameter for determining the strength of the super-exchange interaction between the tetrahedral (A) and octahedral (B) sites. It is observed thatθ_1 decreases from 121.35° to 120.78° as Cobalt concentration increases. This slight reduction indicates a deviation from the ideal geometry, suggesting that the super-exchange path is becoming more "bent." This structural modification is expected to influence the magnetic

properties, such as the saturation magnetization (Ms) and Neel temperature (T_N). The bond angle θ_2 (B-O-B) represents the interaction between the octahedral cations. The value of $\theta_2$shows an increasing trend from 93.68° to 94.25°. In an ideal spinel lattice, this angle is typically 90°; however, in inverse spinels, the presence of larger Co^{2+} ions at the B-site induces a local expansion of the octahedral framework. The increase in $\theta_2$confirms an increase in the trigonal distortion of the octahedral sites, which further minimizes the potential energy of the lattice. The variations in the angles θ_3,θ_4,θ_5 are also consistent with the increasing oxygen parameter (u). The marginal increment in θ_3 (B-O-B) and the adjustments in θ_4 and θ_5 signify a systematic rearrangement of the oxygen framework to accommodate the internal strain caused by the substitution of Co^{2+}.

The systematic variation in these bond angles, coupled with the contraction in bond lengths d_A and d_B, validates the formation of a highly strained yet stable nanocrystal line spinel structure. The increasing trigonal distortion at the B-sites and the modification of the A-O-B super-exchange angles are indicative of the complex interplay between cation redistribution and lattice contraction in the $Co_xFe_{(3-x)}O_4$ system.

3.2.6 Theoretical Estimation of Magnetic Parameters using Néel's Sublattice Model

In order to understand the magnetic behavior of the $Co_xFe_{(3-x)}O_4$system without direct VSM measurements, the net magnetic moment (n_B) and saturation magnetization (Ms) were theoretically estimated using Néel's two-sublattice model[27-.29]. The cation distribution was used to calculate the magnetic moments of the tetrahedral (M_A) and octahedral (M_B) sites[30]. The $Co_xFe_{(3-x)}O_4$ is an inverse spinel configuration hence in cation distribution of this configuration Fe^{3+} ions occupy both tetrahedral (A) and octahedral (B) sites, whereas Co^{2+} ions preferentially occupy the octahedral (B) sites. The relative occupancy of Co^{2+} ions at B-sites increases, with increasing cobalt concentration which affects the magnetic and structural behavior of the system. The cation distribution for the current series is represented as;

$(Fe^{3+})_A\ [Co_x^{2+}\ Fe_{2-x}^{3+}]_B\ O_4^{2-}$.

"The theoretical magnetic moments for the constituent ions, determined by their unpaired electron spin states, are $5\mu_B$ for Fe^{3+} ion and $3\mu_B$ for Co^{2+} ion.

The total magnetic moment for each sublattice is calculated by summing the contributions of the ions residing at each site;

Tetrahedral Sublattice (M_A): As the A-site is entirely occupied by one Fe^{3+} ion per formula unit $M_A = 1 \times\mu(Fe^{3+}) = 5.0\mu_B$

Octahedral Sublattice (M_B): The B-site contains a mixture of $Co^{2+}$and the remaining Fe^{3+}ions:

$M_B = x \times\mu(Co^{2+}) + (2-x) \times\mu(Fe^{3+})$

$M_B = 3x\mu_B + 5(2-x)\mu_B = (10 - 2x)\ \mu_B$

According to Néel's theory, the magnetic moments of the A and B sublattices are aligned anti-parallel to each other. The net magnetic moment (n_B) in Bohr magnetons (μ_B) is given by;

$n_B = M_B - M_A$
$n_B=(10 - 2x)\ \mu_B - 5.0\mu_B$
$n_B = (5 - 2x)\ \mu_B$

The saturation magnetization (Ms) is subsequently calculated using the relation;

$$M_s = \frac{5585\, n_B}{M_w} \quad \text{... (7)}$$

(where M_w is the molecular weight of the respective composition).

The calculated A- and B –sublattice magnetic moments, net magnetic moment, and theoretically estimated saturation magnetization are summarized in Table 8.

The theoretical investigation using Néel's two-sublattice model reveals a systematic decrease in the net magnetic moment (n_B) from $4.00\mu_B$ to $3.80\mu_B$ as the cobalt concentration (x) increases from 0.50 to 0.60. This trend is mathematically attributed to the substitution of high-moment Fe^{3+} ions ($5\mu_B$) with relatively lower-moment Co^{2+} ions ($3\ \mu_B$) in the octahedral[B] sites, which reduces the overall magnetization of the spinel lattice[31].

Table 8 — Theoretically Estimated Magnetic Parameters

Samples x	M_A (μ_B)	M_B (μ_B)	n_B(μ_B)	M_w(g/mole)	Ms (emu/g)
0.50(S_1)	5.0	9	4.0	233.09	95.84
0.55(S_2)	5.0	8.9	3.9	233.24	93.38
0.60(S_3)	5.0	8.8	3.8	233.40	90.93

3.2.7 Thermal Stability of Magnetic Order (Curie Temperature, T_C)

The Curie Temperature (T_C), which defines the transition from a ferrimagnetic to a paramagnetic state, was theoretically estimated based on the molecular field theory[32].

$$Tc = (M \times n_B \times \mu_B) / (3 \times k_B) \text{ and} \frac{\mu_B}{K_B} = 0.677\ K/T$$

where M is Molecular Field Constant and given by $M \propto \frac{1}{(d_A+d_B)^{10}}$

The Molecular Field Constant (M) used in the estimation of the Curie Temperature (T_C) was determined based on the Néel's Molecular Field Theory and calibrated using the experimental structural data[33]. In spinel ferrites, M represents the strength of the internal exchange field and is sensitive to the inter-ionic distances. In the present study, the Molecular Field Constant (M) was taken in the range of 833.05 T to 909.12 T for the $Co_xFe_{3-x}O_4$ (x = 0.50, 0.55, 0.60) series using above formula. The systematic increase in the value of M from 833.05 T (x=0.50) to 909.12 T (x=0.60) is directly correlated with the observed lattice contraction from 8.383 Å to 8.313 Å. The calculated values show a consistent rise in (T_C), from 745.34 K, 758.95 K and 772.18 K as the Cobalt substitution (x) increases from 0.50 to 0.60. This upward trend is a direct result of the enhanced A-O-B super-exchange interaction. As the lattice contracts (8.383 Å → 8.313 Å), the overlap of electronic orbitals between the magnetic cations and oxygen ions increases, requiring more thermal energy to disrupt the magnetic alignment. The higher T_C for the x = 0.60 sample confirms its superior thermal stability, making it highly suitable for applications involving high-frequency or high-temperature environments. The composition-dependent molecular-field constants and the corresponding estimated Curie temperatures are summarized in Table 9.

Table 9 — Consolidated Calculation table for Curie Temp (T_C)

Sample (x)	Sum of Bond Lengths (d_A+d_B)	Molecular Field (M) (T)	Curie Temp (T_C) (K)
0.50 (S1)	3.964 Å	833.05	745.34
0.55 (S2)	3.952 Å	871.40	758.95
0.60 (S3)	3.937 Å	909.12	772.18

3.2.8 Estimation of Debye Temperature (θ_D) and Lattice Rigidity

The mechanical and thermal stability of the $Co_xFe_{(3-x)}O_4$ system is further evaluated through the estimation of the Debye Temperature (θ_D)[34]. The Debye temperature is a fundamental parameter that correlates the elastic properties with the lattice vibrations (phonons) and provides a quantitative measure of the atomic bonding strength within the spinel framework. The calculated Debye Temperature θ_D (K) shows a marginal but consistent increase from 485.5 K to 485.7 K, indicating a slight enhancement in the lattice rigidity as Co-content increases as shown in Table 10."

Physically, a higher θ_D (K) suggests that the atoms are more 'tightly bound' within the unit cell, leading to reduced lattice vibrations and enhanced thermal stability. This observation is in perfect agreement with the Lattice Contraction (8.383 Å → 8.313 Å) observed in XRD. As the inter-atomic distances decrease, the atomic bonds become stiffer, making the x = 0.60 sample the most mechanically robust and thermally stable composition in this series. A consolidated comparison of the principal structural, elastic, magnetic and thermal parameters and their trends with cobalt content is provided in Table 11.

3.3 Microstructural and Elemental Analysis

3.3.1 Morphological Study (SEM)

The SEM micrographs of samples S1 (x = 0.50), S2 (x = 0.55), and S3 (x = 0.60) at different magnifications are presented in Fig. 4 (a–f), where Fig. 4 (a, b), 4 (c, d), and 4 (e, f) correspond to S1, S2, and S3, respectively.

The micrographs reveal highly agglomerated and irregularly shaped grains for all samples, which is a typical characteristic of ferrites synthesized via the sol–gel auto-combustion method due to rapid combustion and gas evolution. In sample S1, larger flake-like clusters with significant porosity and voids are observed, indicating loosely packed agglomerates[35].

With increasing cobalt substitution (S2 and S3), the morphology exhibits comparatively finer and more compact grain distribution. Although agglomeration persists due to magnetic interactions among particles, the microstructure becomes relatively more homogeneous with reduced cluster size and improved packing.

Table 10 — Calculated thermal parameters calcined at 600 °C (optimized conditions)

Samples (x)	a (Å)	M (g/mol)	ρx (kg/m³)	V_l (m/s)	V_t (m/s)	Vm (m/s)	θ_D (K)
0.50 (S1)	8.383	233.09	5253	5325.2	3037.0	3381.1	485.5
0.55 (S2)	8.352	233.24	5315	5305.2	3023.9	3366.8	485.6
0.60 (S3)	8.313	233.40	5394	5278.8	3009.4	3350.6	485.7

The grain size estimated from the SEM micrographs lies in the range of ~400–800 nm, showing a decreasing trend from S1 to S3. This is significantly larger than the crystallite size (~46 nm) obtained from XRD analysis, indicating that the observed grains are agglomerated secondary particles formed by the clustering of multiple Nanosized crystallites. Such behavior is commonly attributed to high surface energy and inter-particle magnetic interactions in ferrite systems.

Table 11 — Summary of Mechanical, Elastic, Magnetic, Electrical & thermal Properties Analysis

Parameter	Trend with x	Underlying Cause
Lattice Parameter (a)	Decreasing	Cation Size & Compactness
Bond Lengths (d)	Decreasing	Unit Cell Contraction
Stiffness (E, B, G)	Increasing	Tight Inter-atomic Bonding
Magnetization (Ms)	Decreasing	Cation Redistribution & Spin Canting
Conductivity (σ_{AC})	Increasing	Reduced Hopping Distance
Curie Temperature, T_C	Increasing	Stronger A-O-B super-exchange interaction
Debye Temperature (θ_D) (k)	Increasing	Increased Lattice Rigidity

Furthermore, the relatively larger grain size can be attributed to the high calcination temperature (600 °C), which promotes atomic diffusion, grain growth, and coalescence of smaller crystallites into larger clusters, resulting in improved crystallinity along with increased particle size.

3.3.2 Elemental Compositional Analysis (EDX)

The elemental purity and stoichiometric composition of the synthesized $Co_xFe_{(3-x)}O_4$ (x = 0.50, 0.55, 0.60) nanoparticles were validated using Energy Dispersive X-ray (EDX) analysis[36]. The EDX spectra along with their corresponding elemental weight and atomic percentage tables are presented in Fig. 5 (a–f).

The analysis confirms the presence of Cobalt (Co), Iron (Fe), and Oxygen (O) as the primary constituents in all samples. For the x = 0.50 composition (Sample 1), the atomic percentages of Fe and Co were found to be 32.35 % and 17.65 %, respectively. As the substitution level increased to x = 0.55 (Sample 2), a corresponding rise in the Cobalt atomic percentage to 19.21 % was observed, confirming the successful incorporation of Co ions into the spinel lattice. For the x = 0.60 sample, the elemental proportions remained consistent with the expected stoichiometric ratios. No

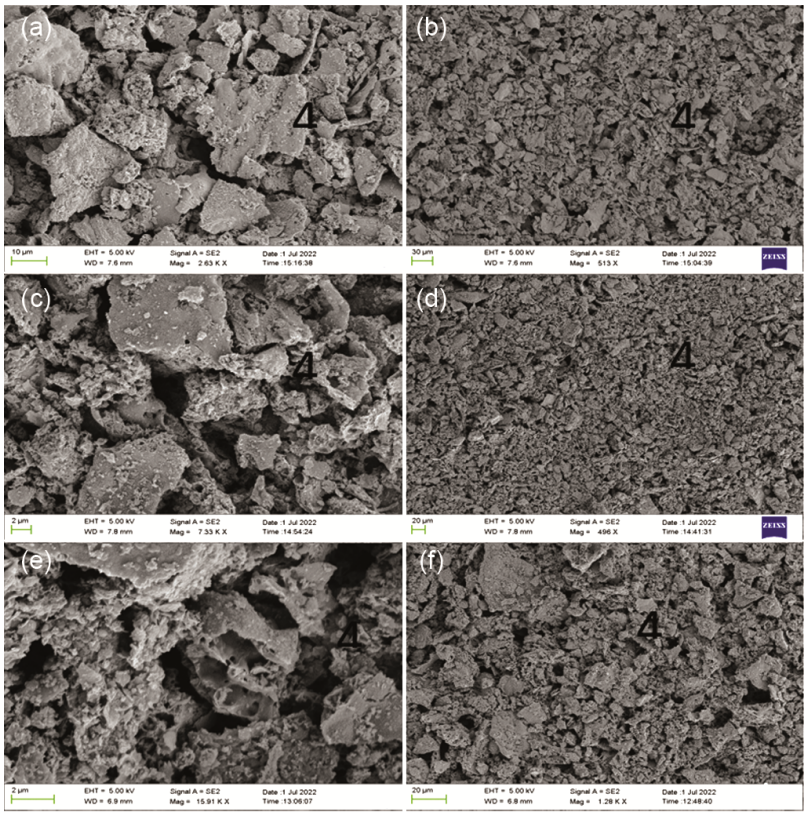

Fig. 4 — Representative SEM micrographs of nanoparticles: (a, b) for x = 0.50, (c, d) for x = 0.55 and (e, f) for x = 0.60 and calcined at 600 °C (optimized conditions)

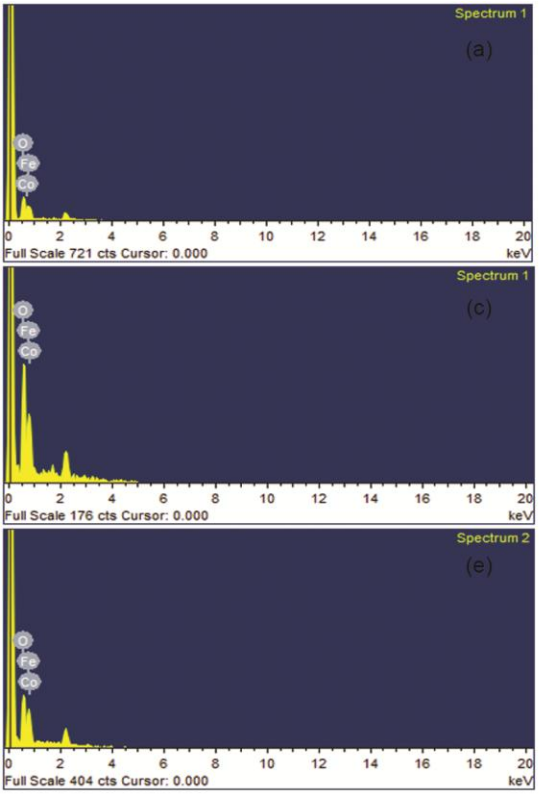

Element	Weight%	Atomic%	Compd%	Formula
				(b)
Fe L	49.54	32.35	63.73	FeO
Co L	28.53	17.65	36.27	CoO
O	21.94	50.00		
Totals	100.00			

Element	Weight%	Atomic%	Compd%	Formula
				(d)
Fe L	47.09	30.79	60.58	FeO
Co L	31.00	19.21	39.42	CoO
O	21.91	50.00		
Totals	100.00			

Element	Weight%	Atomic%	Compd%	Formula
				(f)
Fe L	48.85	31.91	62.85	FeO
Co L	29.22	18.09	37.15	CoO
O	21.93	50.00		
Totals	100.00			

Fig. 5 — EDX spectra and corresponding elemental composition tables of $Co_xFe_{(3-x)}O_4$ nanoparticles: (a, b) for x = 0.50, (c, d) for x = 0.55, and (e, f) for x = 0.60. The data confirms stoichiometric accuracy and high elemental purity calcined at 600 °C (optimized conditions)

additional peaks related to any secondary phases or external impurities were detected in the spectra, signifying the high chemical purity of the precursors and the effectiveness of the sol-gel auto-combustion route. The oxygen content remained stable at 50.00 % (atomic) across all compositions, confirming the formation of a well-balanced oxide phase. These results are in excellent agreement with the XRD data, further solidifying the successful synthesis of the $Co_xFe_{(3-x)}O_4$ nano-ferrite system.

4 Conclusion

The present study shows the successful synthesis and investigation of cobalt-substituted nano-ferrites, $Co_xFe_{(3-x)}O_4$ (x = 0.50, 0.55, 0.60), through the sol–gel auto-combustion method. Single-phase cubic spinel structure is confirmed by X-ray diffraction analysis with a gradual decrease in lattice constant from 8.383 Å to 8.313 Å, indicating lattice contraction with increasing cobalt content. Williamson–Hall analysis reveals a reduction in crystallite size from 46.2 nm to 27.7 nm along with an increase in micro strain which suggests enhanced lattice distortion and defect concentration.

The structural stability of the cubic spinel lattice is confirmed by calculating tolerance factor (0.643–0.639). The interatomic distances and stronger bonding interactions within the lattice are confirmed by the increase in elastic constants and Young's modulus with cobalt substitution. The theoretically estimated net magnetic moment and saturation magnetization based on Néel's two-sublattice model indicate a slight decrease with increasing cobalt concentration. This is due to the substitution of Fe^{3+} ions by lower magnetic moment Co^{2+} ions at the octahedral sites. However, enhanced thermal stability of magnetic order is suggested by estimated Curie temperature which shows an increasing trend, scanning electron microscopy reveals highly agglomerated morphology with grain sizes in the range of ~400–800 nm, significantly larger than the crystallite size obtained from XRD, confirming the formation of secondary agglomerated particles composed of multiple nanoscale crystallites. A gradual reduction in grain size with increasing cobalt content indicates improved microstructural uniformity.

Furthermore, the surface-to-volume ratio, calculated from the XRD-derived crystallite size, increases with cobalt content due to size reduction, indicating a higher fraction of surface atoms.

Overall, the study establishes a clear correlation between compositional variation, lattice contraction, microstructural evolution, and theoretically estimated physical properties, suggesting that these nano-ferrites may be suitable for applications requiring structurally stable and thermally robust magnetic materials.

References

1 Goldman A, Modern Ferrite Technology, 2nd Edn, (Springer Science & Business Media, New York) 2006.
2 Pathak T K, Vasoya N H, Lakhani V K & Modi K B, *Ceram Int*, 41 (2015) 110.
3 Verwey E J W & Heilmann E L, *J Chem Phys*, 15 (1947) 174.
4 Yue Z, Zhou J, Li L & Gui Z, *J Magn Magn Mater*, 233 (2001) 224.
5 Hwang C C & Wu J S, *J Mater Sci*, 39 (2004) 3111.
6 Vaishnava P P, Senaratne U, Buc E, Naik R, Naik V M, Tsoi G & Wegner P P, *J Appl Phys*, 102 (2007) 064314.
7 Wooster W A, A Textbook on Crystal Physics, (Cambridge University Press, London) 1938.
8 Ravinder D, *J Appl Phys*, 75 (1994) 6118.
9 Adil Y, Ahmed M A & El-Bordany S T, *J Sol-Gel Sci Technol*, 94 (2020) 412.
10 Slatineanu T, Iordan A, Palamaru M N, Caltun O F, Gaenton V & Leontie L, *Mater Res Bull*, 47 (2012) 2720.
11 JCPDS Card No. 22-1086, Standard Diffraction Data for Cubic Spinel Cobalt Ferrite, (International Centre for Diffraction Data, Swarthmore, PA) 1972.
12 Scherrer P, *Math Phys Kl*, 1918 (1918) 98.
13 Cullity B D & Stock S R, Elements of X-Ray Diffraction, 3rd Edn, (Prentice Hall, New Jersey) 2001.
14 Nelson J B & Riley D P, *Proc Phys Soc*, 57 (1945) 160.
15 Williamson G K & Hall W H, *Acta Metall*, 1 (1953) 22.
16 Sudakar C, Subbanna S & Kutty T R N, *J Magn Magn Mater*, 263 (2003) 253.
17 Williamson G K & Smallman R E, *Philos Mag*, 1 (1956) 34.
18 Smallman R E & Westmacott K H, *Philos Mag*, 2 (1957) 669.
19 Poole Jr C P & Owens F J, Introduction to Nanotechnology, (John Wiley & Sons, New Jersey) 2003.
20 Harris G B, *Philos Mag*, 39 (1948) 113.
21 Goldschmidt V M, *Naturwissenschaften*, 14 (1926) 477.
22 Shannon R D, *Acta Crystallogr Sect A*, 32 (1976) 751.
23 Smit J & Wijn H P J, Ferrites, (Philips Technical Library, Eindhoven) 1959.
24 Koops C G, *Phys Rev*, 83 (1951) 121.
25 Waldron R D, *Phys Rev*, 99 (1955) 1727.
26 Buerger M J, Crystal-Structure Analysis, (John Wiley & Sons, New York) 1960.
27 Gorter E W, *Philips Res Rep*, 9 (1954) 295.
28 Néel L, *Ann Phys*, 12 (1948) 137.
29 Upadhyay C, Mishra D, Verma S, Anand S & Verma R P, *J Magn Magn Mater*, 280 (2004) 31.
30 Standley K J, Oxide Magnetic Materials, 2nd Edn, (Clarendon Press, Oxford) 1972.
31 Tahir S, Anis-ur-Rehman M & Bhatti A S, *J Magn Magn Mater*, 432 (2017) 298.
32 Ishikawa T, *J Phys Soc Jpn*, 13 (1958) 128.
33 Upadhyay R V & Mehta R V, Pramana – *J Phys*, 41 (1993) 421.
34 Kittel C, Introduction to Solid State Physics, 8th Edn, (John Wiley & Sons, New York) 2005.
35 Goldstein J I, Newbury D E, Michael J R, Ritchie N W, Scott J H J & Joy D C, Scann Electr Microscopy X-Ray Microanalysis, 4th Edn, (Springer, New York) 2017.
36 Newbury D E & Ritchie N W, *Scan*, 35 (2013) 141.